10. The sizes of the terrestrial sources and sinks can be estimated by solving for the values of α_j that minimize the sum

$$\chi^2 = \sum_{j=1}^{q} [B(x_j) + O(x_j) + F(x_j) + R(x_j) - S(x_j)]^2 \quad (2)$$

where q is the number of atmospheric sampling stations. In practice, it is convenient to reference all concentrations in the sum of squares to the value at the South Pole, and then solve for the values of α by using singular value decomposition [W. H. Press, B. R. Flannery, S. A. Teukolsky, W. T. Vetterling, *Numerical Recipes* (Cambridge Univ. Press, New York, 1992)] with a mass conservation constraint [G. H. Golub and C. F. V. Loan, *Matrix Computations* (Johns Hopkins Univ. Press, Baltimore, 1990)] that requires the terrestrial biosphere to balance all the other sources minus sinks.

11. J. D. Mahlman and W. J. Moxim, *J. Atmos. Sci.* **35**, 1340 (1978); H. Levy, J. D. Mahlman, W. J. Moxim, *J. Geophys. Res.* **87**, 3061 (1982).
12. Meridional and vertical transport in both GCTM and SKYHI have been evaluated against observations of radon-222, krypton-85, and CFC-11. The original comparison with radon-222 observations led to the implementation of a more aggressive vertical mixing scheme in SKYHI that improved the simulation of this tracer. A recent model comparison study with SF_6 shows that both SKYHI and GCTM do well at simulating marine boundary-layer concentrations, although the continental concentrations may be too high (A. S. Denning *et al*., *Tellus*, in press).
13. K. Hamilton, R. J. Wilson, J. D. Mahlman, L. J. Umscheid, *J. Atmos. Sci.* **52**, 5 (1995).
14. J. L. Sarmiento, R. Murnane, C. L. Quéré, *Philos. Trans. R. Soc. London Ser. A* **348**, 211 (1995); R. Murnane, J. L. Sarmiento, C. L. Quéré, *Global Biogeochem. Cycles*, in press.
15. T. Takahashi *et al*., *Proc. Natl. Acad. Sci. U.S.A.* **94**, 8992 (1997).
16. The sea-air flux is calculated by taking the product of the sea-air pCO_2 difference and a climatic wind speed–dependent estimate of the gas exchange flux based on the oceanic inventory of bomb radiocarbon [R. Wanninkhof, *J. Geophys. Res.* **97**, 7373 (1992)]. Most of the difference between OBM and T97 in global oceanic uptake (0.8 Pg C $year^{-1}$) occurs in the tropics and Southern Hemisphere (Table 1), where the spatiotemporal coverage of measurements used in T97 and tracer data used for model evaluation is very uneven. The recent completion of the World Ocean Circulation Experiment will greatly improve the coverage.
17. U. Siegenthaler and J. L. Sarmiento, *Nature* **365**, 119 (1993).
18. R. J. Andres, G. Marland, I. Fung, E. Matthews, *Global Biogeochem. Cycles* **10**, 419 (1996).
19. C. S. Potter *et al*., *ibid.* **7**, 811 (1993). The CASA model does not consider the effect of biomass burning and biospheric emissions of hydrocarbons. Oxidation of hydrocarbons leads to the formation of CO, which is further oxidized to CO_2 in the atmosphere. Because the biomass burning and CO oxidation sources of CO_2 are not modeled, they are effectively treated here as part of the biospheric respiration of CASA.
20. The GLOBALVIEW-CO2 1996 database has a total of 66 stations. Tae-Ahn Peninsula and Westerland were excluded because they are strongly contaminated by local fossil CO_2 sources that are difficult for the coarse resolution models to simulate in sufficient detail. Sable Island was excluded because it appears that the data may have a positive bias (K. Higuchi, personal communication). The following procedures were followed in calculating annual averages of model simulations for comparison with observations. (i) Sampling of models at coastal stations was moved out to sea by one grid cell in order to avoid inadvertent terrestrial contamination resulting from the coarse resolution of the atmospheric general circulation models (GCMs). (ii) All other sampling was done at the nearest grid cell to the station. (iii) Four stations were sampled by wind sectors in order to match as closely as possible the way that the actual sampling is done: Cape Grim, Tasmania (180° to 270°); Cape Meares, Oregon (210° to 330°); Key Biscayne, Florida (30° to 160°); and Mace Head, Ireland (210° to 300°).
21. GLOBALVIEW-CO2, *Cooperative Atmospheric Data Integration Project—Carbon Dioxide* (NOAA/CMDL, Boulder, CO, 1996), CD-ROM; also available via anonymous FTP to ftp.cmdl.noaa.gov, Path: ccg/co2/GLOBALVIEW.
22. K. A. Masarie and P. P. Tans, *J. Geophys. Res.* **100**, 11,593 (1995).
23. M. Gloor, S.-M. Fan, S. Pacala, J. L. Sarmiento, in preparation.
24. P. S. Bakwin, P. P. Tans, D. F. Hurst, C. Zhao, *Tellus*, in press.
25. The mean North Atlantic air-sea pCO_2 difference measured by T97 is 20 ± 5 μatm. Increasing the temperate North Atlantic air-sea flux to 1.4 Pg C $year^{-1}$ would require an increase in the air-sea pCO_2 difference to about 90 μatm, or a 4.5 times increase of the gas exchange coefficient [which is already about twice as large as other commonly used estimates (*17*)], or some combination of the two. Tans *et al*. discussed this issue in their study (*2*). An independent constraint on the North Atlantic sink is the anthropogenic carbon inventory estimate obtained from analysis of observations of dissolved inorganic carbon [N. Gruber, J. L. Sarmiento, T. F. Stocker, *Global Biogeochem. Cycles* **10**, 809 (1996)]. This estimate is almost identical to the OBM simulations (which agree with T97 in the North Atlantic).
26. There was little impact on the estimates when the terrestrial uptake was assumed to be proportional to the heterotrophic respiration in the CASA model (*19*), which has very different temporal patterns from the NPP. In another case, the terrestrial uptake was assumed to be invariable with season and to be uniform within each of five regions (separate boreal and temperate regions in Eurasia–North Africa and North America, and the rest of land surfaces combined). The estimates of total terrestrial uptake for North America and for Eurasia–North Africa were well constrained and remained essentially unchanged from those shown in Table 2 (averaged over the four cases) even with this radical assumption.
27. M. Williams, in *World Deforestation in the Twentieth Century*, R. J. Richards and R. P. Tucker, Eds. (Duke Univ. Press, Durham, NC, 1988), pp. 211–229; K. Power, personal communication.
28. S. C. Wofsy *et al*., *Science* **260**, 1314 (1993); M. L. Goulden, J. W. Munger, S. M. Fan, B. C. Daube, S. C. Wofsy, *ibid.* **271**, 1576 (1996); S. Greco and D. D. Baldocchi, *Global Change Biol.* **2**, 183 (1996).
29. M. L. Goulden, J. W. Munger, S.-M. Fan, B. C. Daube, S. C. Wofsy, *Science* **279**, 214 (1998).
30. R. A. Birdsey *et al*., *USDA Forest Service, Productivity of America's Forests and Climate Change* (1995); D. P. Turner, G. J. Koerper, M. E. Harmon, J. J. Lee, *Ecol. Appl.* **5**, 421 (1995).
31. D. Schimel *et al*., in *Climate Change 1995*, J. T. Houghton *et al*., Eds. (Cambridge Univ. Press, Cambridge, 1996), pp. 76–86
32. R. F. Stallard, *Global Biogeochem. Cycles* **12**, 231 (1998).
33. J. M. Melillo, I. C. Prentice, G. D. Farquhar, E.-D. Schulze, O. E. Sala, in (*31*), pp. 447–481.
34. D. W. Schindler and S. E. Bayley, *Global Biogeochem. Cycles* **7**, 717 (1993); R. J. M. Hudson, S. A. Gherini, R. A. Goldstein, *ibid.* **8**, 307 (1994); A. R. Townsend, B. H. Braswell, E. A. Holland, J. E. Penner, *Ecol. Appl.* **6**, 806 (1996); E. A. Holland *et al*., *J. Geophys. Res.* **102**, 15849 (1997).
35. N. Nicholls, *et al*., in (*31*), pp. 133–192; R. B. Myneni, S. O. Los, C. J. Tucker, *Geophys. Res. Lett.* **23**, 729 (1996).
36. A. Dai, I. Y. Fung, *Global Biogeochem. Cycles* **7**, 599 (1993).
37. This research was carried out as part of the Carbon Modeling Consortium (CMC), which is supported by the Office of Global Programs and Geophysical Fluid Dynamics Laboratory of the NOAA. We acknowledge support from the Department of Energy. Stimulating discussions with our colleagues in the CMC and elsewhere is gratefully acknowledged, with particular appreciation to P. Bakwin, D. Baker, and M. Bender. L. Bruhwiler, R. Hemler, H. Levy, and W. Moxim provided advice on the GCTM and SKYHI simulations, T. Hughes helped access the OBM results, and C. Field provided the CASA simulation results.

29 May 1998; accepted 15 September 1998

North Atlantic Oscillation Dynamics Recorded in Greenland Ice Cores

C. Appenzeller,* T. F. Stocker, M. Anklin

Carefully selected ice core data from Greenland can be used to reconstruct an annual proxy North Atlantic oscillation (NAO) index. This index for the past 350 years indicates that the NAO is an intermittent climate oscillation with temporally active (coherent) and passive (incoherent) phases. No indication for a single, persistent, multiannual NAO frequency is found. In active phases, most of the energy is located in the frequency band with periods less than about 15 years. In addition, variability on time scales of 80 to 90 years has been observed since the mid-19th century.

The North Atlantic oscillation (NAO) is one of the Northern Hemisphere's major multiannual climate fluctuations and typically is described with an index based on the pressure difference between Iceland and the Azores (*1*). On multiannual time scales, variations in the NAO have a strong impact on North Atlantic and European climate (*2*) and also on the recent surface temperature warming trend in the Northern Hemisphere (*3*). In recent decades the winter index remained predominantly in a positive state, and there is evidence that during this period the variability might have increased (*4*). Analysis of various NAO indices (*5*) showed

C. Appenzeller and T. F. Stocker, Climate and Environmental Physics, University of Bern, Sidlerstrasse 5, CH-3012 Bern, Switzerland. M. Anklin, Department of Hydrology and Water Resources, University of Arizona, Tucson, AZ 85721, USA.

*To whom correspondence should be addressed. E-mail: christof.appenzeller@climate.unibe.ch

maximum amplitudes in the frequency bands of about 2, 7 to 8, 20, and 70 years, but none of these peaks is strongly statistically significant. A longer NAO time series can provide more reliable information about the nature of NAO variability and possible dominant time scales associated with this climate oscillation. This information is necessary for both testing theoretical and numerical models and quantifying natural and anthropogenic changes in NAO behavior.

A number of proxy data such as historical records (*6*), tree ring data (*7*), and ice core data (*8*) potentially can be used to estimate long-term NAO variability. Here we reconstruct an annually averaged proxy index from Greenland ice accumulation rates. The correlation between ice accumulation and NAO was shown (*9*) to be strongly negative in western Greenland, whereas it was weak in central Greenland. The data used for the reconstruction were measured on the NASA-U core (*10*) located in western Greenland at 73.84°N and 49.49°W and 2370 m above sea level. The annual mean temperature is about −27°C and summer melt layers are formed rarely. A quality check of the record against two shorter neighboring cores shows (*11*) that the multiannual variability recorded in the core can be taken as representative for that region after the high-frequency part is removed.

The correlation between net snow accumulation at the NASA-U drill site and the mean sea level pressure distribution over the entire North Atlantic region is illustrated in Fig. 1. Both data sets are based on 15 years of monthly mean ECMWF (European Centre for Medium-Range Weather Forecasts) reanalysis data (*9, 12*). The pattern of explained pressure variation by 1 SD in snow accumulation (scaled with −1.0) shows a clear dipole over the Atlantic that strongly resembles the NAO pattern, with negative values over Iceland and positive values at lower latitudes. Thus, it can be expected that the variability of the measured NASA-U ice accumulation rates also reflects the variability of the NAO index.

In Fig. 2 the proxy NAO index derived from the normalized annual mean ice accumulation rates over the entire ~350 years (shaded) is compared with the measured annual mean NAO index for the past 130 years (*1, 13*) (solid line). In both data sets the linear trend and the high-frequency part are removed (*11*). The correlation coefficient between the two indices is 0.57; hence, about one-third (0.57^2) of the total variability is explained by a linear relationship. Correlation coefficients with other commonly used NAO indices were also determined (Table 1), showing that the proxy index also captures a good part of the winter index variability. The lowest correlation is found with reconstructed winter NAO variability from tree-ring widths (*14*). Our proxy index shows particularly low values around 1880, whereas the highest values are around 1695. Periods with a persistently low index (Fig. 2, thin line) occurred in the second half of the 19th century and also around 1950 to 1975 and 1675 to 1690 (Maunder minimum). Persistently positive anomalies are found in the early 18th and early 20th centuries. From 1975 to 1990 the proxy index appears to underestimate the increase in the NAO index; however, it should be noted that these periods correspond to the top meters of the ice core, where the equivalent accumulation analysis is difficult because of uncertainties in density measurements.

To explore the dynamics of the NAO index, we used a Morlet wavelet analysis (*15, 16*) instead of a classic Fourier analysis. The statistical significance of the local wavelet power spectrum was tested by a Monte Carlo method. Our null hypothesis states that the NAO index is an autoregressive (AR-1) noise time series with autocorrelation coefficient α estimated from the observed data. Both time series, the proxy index as well as the instrumental index, are nearly white with $\alpha = -0.1$ and $+0.1$, respectively.

The local wavelet spectrum of the proxy NAO index (Fig. 3A) shows a number of time sequences with spectral power above the 90 and 95% confidence levels. The most pronounced sequences occur during 1685 to 1720, 1730 to 1775, 1870 to 1900, and 1900 to 1930; a weaker phase has prevailed from 1960 onward. The spectrum does not show one or more dominant and persistent NAO frequencies throughout the

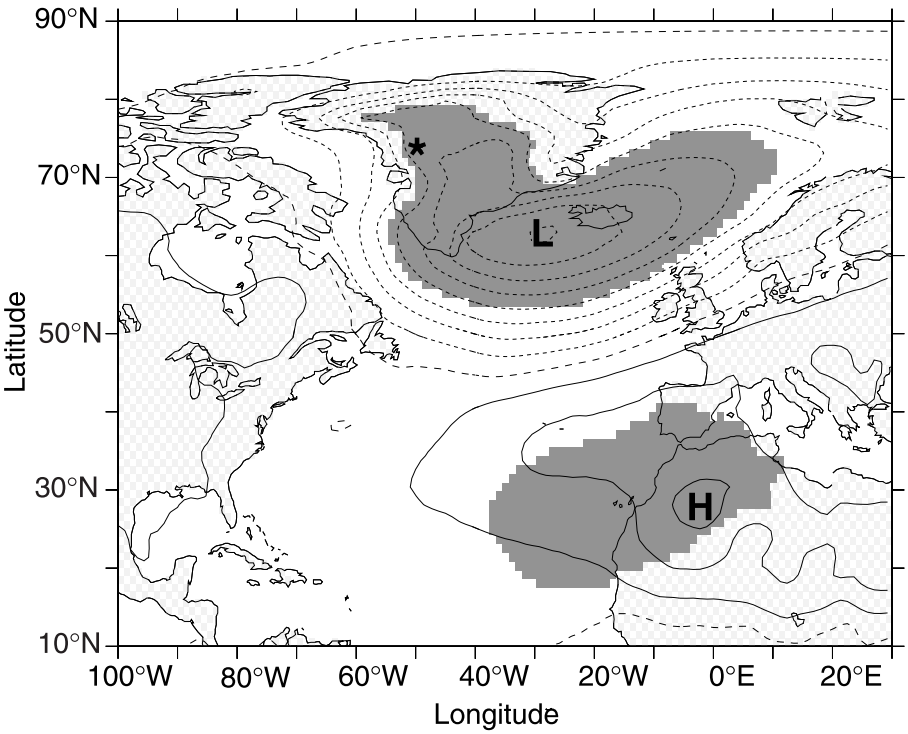

Fig. 1. Teleconnection map between snow accumulation at the NASA-U drill site (*) and mean pressure at sea level. Contours indicate pressure variation associated with 1 SD in snow accumulation. Contour interval is 0.5 hPa and for clarity values are scaled with −1.0. Long dashed line is the zero line. Regions with statistically significant correlation (above 99% confidence level according to Student's *t* test) are shaded. Both data sets are monthly mean ECMWF reanalysis (*9, 12*) data for 1979–1993.

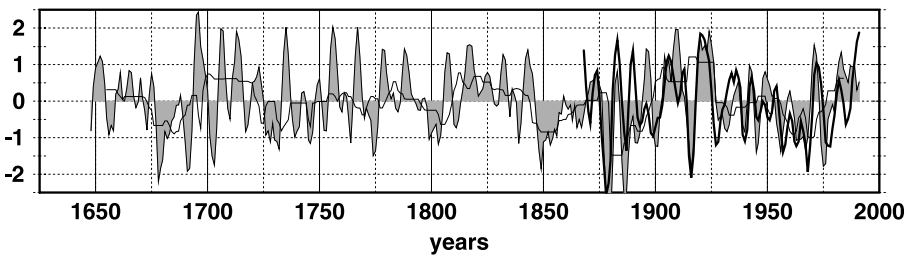

Fig. 2. Normalized proxy NAO index based on western Greenland ice accumulation rates (shaded) and normalized instrumental NAO index (*1, 13*) (thick line). Data are annual means averaged from spring to spring (*10*). Linear trends and high-frequency parts (*11*) are removed. Also shown is a 15-year running median of the proxy index (thin line).

past 350 years but is characterized by a highly nonstationary behavior. One striking feature is that most of the area with significant coherent oscillation is located in the frequency band of less than 15 years. Maximum power is around 5 to 7, 9 to 11, and 12 to 14 years. In addition, we note that from 1850 onward the proxy NAO index also shows significant (95%) power at 80 to 90 years. Roughly comparable multiannual (*16, 17*) and century scale (*17, 18*) variability was found in a number of independent temperature proxy analyses. This is consistent with the profound effect of NAO-like variability on the northern hemisphere and European surface temperature (*2*, *3*). Note that in the first 200 years of the proxy NAO record no indication of such a century-scale variability is found and that the onset of this oscillation is comparable to that expected from greenhouse gas forcing (*19*).

The local wavelet power spectrum of the measured annual NAO index for the instrumental period (Fig. 3B) shows a number of active phases with maximum amplitude in frequency bands similar to those in the spectrum of the proxy index (Fig. 3A). Although there are some differences, the two local wavelet power spectra are similar and indicate that our proxy NAO index correctly reproduces the multiannual variability exhibited by the instrumental annual NAO index.

A number of mechanisms have been proposed to explain NAO-like variability, including uncoupled and coupled atmosphere-ocean interactions (*20*). For a truly internally or externally forced climate oscillation, one would expect to see statistically significant wavelet power throughout most of the 350 years indicated in Fig. 3A, although the dominant frequency might change in time (*21*). In contrast, the observed power spectrum of the proxy index suggests that the NAO is an intermittent climate oscillation characterized by temporally active (coherent) and passive (incoherent) phases. Atmosphere-ocean interaction on the typical time scales of 5 to 15 years might occur during active phases but would be absent during passive phases, although spatially coherent patterns still may exist. Note that we cannot exclude the possibility that the proxy NAO index represents simply stochastic variability. Monte Carlo simulations based on a large number of autoregressive noise time series with the same autocorrelation coefficient as the proxy index showed (*22*) that randomly distributed active and passive sequences with wavelet spectra above the 95% significance level can also occur by chance.

Our study shows that it is possible to reconstruct a proxy NAO index from carefully selected Greenland ice core data and that intermittency is an important feature in the NAO for the past 350 years. If this intermittency is not simply caused by a stochastic process, it may have implications for climate prediction in the Atlantic region and Europe (*23*), because the predictability should be increased during coherent active NAO phases.

Table 1. Correlation coefficients between proxy NAO and other common NAO indices. In all data the linear trend and the high-frequency variability are removed (*11*). Annual means are averaged from spring to spring (*13*). Hurrell annual and winter indices (*1, 13*), based on instrumental data, are for 1865–1994. Jones early instrumental NAO index (*6, 13*) is for 1825–1994 and 1865–1994 (in parentheses); Cook tree-ring reconstructed winter mean index (*7*) is for 1701–1980 and 1865–1980 (in parentheses).

	Annual Hurell	Winter Hurrell	Annual Jones	Winter Cook
Proxy NAO	0.57	0.52	0.42 (0.53)	0.14 (0.24)

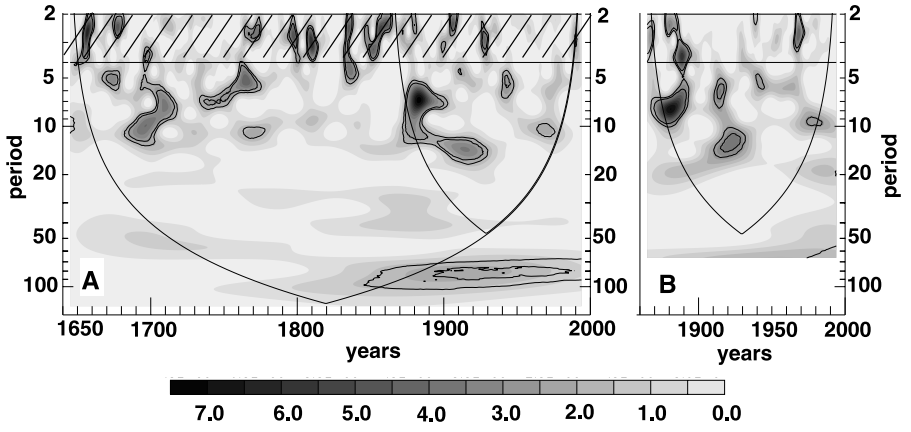

Fig. 3. Local wavelet power spectrum for the proxy NAO index (**A**) and for the instrumental NAO index (**B**) as in Fig. 2, based on a Morlet wavelet with a characteristic frequency of six calculated as described in (*15*). Amplitudes are scaled with the variance of the respective index; hence, the expected power of white noise is 1. Logarithmic vertical axes indicate equivalent periods, and horizontal axes indicate time. The 90 and 95% confidence limits are shown as thin lines, and the cone of influence marks regions where edge effects might underestimate the amplitudes. Hatched region indicates periods for which the proxy index should not be interpreted.

References and Notes

1. J. W. Hurrell, *Science* **269**, 676 (1995). The annual NAO index is defined as the normalized pressure difference between Stykkisholmur, Iceland, and Ponta Delgada, Azores.
2. A large number of atmospheric and oceanic key quantities show variability potentially linked to the NAO. Examples are the series of cold winters in Europe in the 1960s and the variability in surface pressure in the North Atlantic [G. T. Walker and E. W. Bliss, *Mem. R. Meteorol. Soc.* **IV**, 53 (1939); J. M. Wallace and D. S. Gutzler, *Mon. Weather Rev.* **109**, 784 (1981)], in the averaged central-northern European temperature [H. VanLoon and J. C. Rogers, *ibid.* **106**, 296 (1978); C. K. Folland, T. R. Karl, K. Y. Vinnikov, in *Scientific Assessment of Climate Change*, J. T. Houghton, Ed. (IPCC, Cambridge Univ. Press, Cambridge, 1990), pp. 195–242], in the strength of the polar vortex [J. Perlwitz and H.-F. Graf, *J. Clim.* **8**, 2281 (1995); D. W. J. Thompson and J. M. Wallace, *Geophys. Res. Lett.* **25**, 1297 (1998)], in the sea surface temperature [C. Deser and M. L. Blackmon, *J. Clim.* **6**, 1743 (1993); R. T. Sutton and M. R. Allen, *Nature* **388**, 563 (1997)], and in the oceanic northward mass transport [M. McCartney, *Nature* **388**, 521 (1997); R. A. Kerr, *Science* **275**, 754 (1997)].
3. J. W. Hurrell, *J. Geophys. Res.* **23**, 665 (1996).
4. CLIVAR, *A Research Program on Climate Variability and Prediction for the 21st Century*. H. Grassl, Ed. (World Climate Research Programme, Hamburg, 1997).
5. J. C. Rogers, *Mon. Weather Rev.* **112**, 1999 (1984); J. W. Hurrell and H. Van Loon, *Clim. Change* **36**, 301 (1997); E. R. Cook, R. D. D'Arrigo, K. R. Briffa, *Holocene* **8**, 9 (1998).
6. P. D. Jones, T. Jonsson, D. Wheeler, *Int. J. Climatol.* **17**, 1433 (1997).
7. R. D. D'Arrigo, E. R. Cook, G. C. Jacoby, K. R. Briffa, *Q. Sci. Rev.* **12**, 431 (1994); E. R. Cook, R. D. D'Arrigo, K. R. Briffa, *Holocene* **8**, 9 (1998).
8. L. K. Barlow, J. W. C. White, R. G. Barry, J. C. Rogers, P. M. Grootes, *Geophys. Res. Lett.* **20**, 2901 (1993); D. A. Meese *et al.*, *Science* **266**, 1680 (1994); J. W. C. White *et al.*, *J. Geophys. Res.* **102**, 26425 (1997).
9. C. Appenzeller, J. Schwander, S. Sommer, T. F. Stocker, *Geophys. Res. Lett.* **25**, 1939 (1998).
10. M. Anklin, R. C. Bales, E. Mosley-Thompson, K. Steffen, *J. Geophys. Res.*, in press.
11. Ice accumulation rates measured on a single core have a large portion of noise (for example, because of redistribution of snow by wind or subannual timing uncertainties). Two neighboring cores were drilled 50 m and 2 km away from the main core covering the period 1965 to 1993. For the raw accumulation rates, the correlation coefficients between main core and neighboring core are 0.71 and 0.27, respectively. When the high-frequency part is removed (using a standard five-point triangular filter with weights 1, 2, 3, 2, and 1), the correlation coefficients increase to 0.9 and 0.86, respectively. This corresponds to a signal-to-noise ratio of about 7.5 [for definitions, see D. A. Fisher *et al.*, in *Climate Variations and Forcing Mechanisms of the Last 2000 Years*, P. D. Jones, R. S. Bradley, J. Jouzel, Eds. (Springer-Verlag, Berlin, 1996), vol. 41, pp. 297–328]. It also should be noted that any uncertainties in dating the cores could affect the correlation analysis. The effect on the frequency analysis is expected to be small.
12. J. K. Gibson *et al.*, *ERA Description* (ECMWF Re-Analysis Project Report Series, ECMWF, Reading, UK, 1997), vol. 1.
13. Ice accumulation rates and hence the proxy NAO index represent an annual mean averaged from spring to spring. The same averaging period is applied for the instrumental indices. The correlation coefficient between the proxy index and the common annual mean is 0.55 compared with 0.57.
14. A similar lack of correlation was found between

tree-ring index and isotopes measured on the GISP2 ice core [J. W. C. White, D. Gorodetzky, E. R. Cook, L. K. Barlow, in *Climate Variations and Forcing Mechanisms of the Last 2000 Years*, P. D. Jones, R. S. Bradley, J. Jouzel, Eds. (Springer-Verlag, Berlin, 1996), vol. 41, pp. 193–212].
15. C. Torrence and G. P. Compo, *Bull. Am. Meteorol. Soc.* **79**, 61 (1998). For a review, see P. Kumar and E. Foufoula-Georgiou, *Rev. Geophys.* **35**, 385 (1997).
16. S. Baliunas, P. Frick, D. Sokoloff, W. Soon, *Geophys. Res. Lett.* **24**, 1351 (1997).
17. T. F. Stocker and L. A. Mysak, *Clim. Change* **20**, 227 (1992). T. F. Stocker, *NATO ASI* **I44**, 379 (1996).
18. N. Mahasenan, R. G. Watts, H. Dowlatabadi, *Geophys. Res. Lett.* **24**, 563 (1997); M. E. Schlesinger and N. Ramankutty, *Nature* **367**, 723 (1994).
19. M. E. Mann, R. S. Bradley, M. K. Hughes, *Nature* **392**, 779 (1998).
20. Current theoretical and numerical models are reviewed in M. Latif, *J. Clim.* **11**, 602 (1998).
21. T. Delworth, S. Manabe, R. J. Stouffer, *ibid.* **6**, 1993 (1993).
22. Data not shown.
23. S. M. Griffies and K. Bryan, *Science* **275**, 181 (1997).
24. C.A. was supported by the National Swiss Science Foundation (SPPU, CLEAR2). Special thanks to ECMWF; Swiss Met Office (SMA); D. Lüthi, J. W. Hurrell, P. D. Jones, and E. R. Cook for providing their data; and B. Stauffer, J. Schwander, and S. Sommer for fruitful conversations.

29 June 1998; accepted 9 September 1998

Two-Dimensional Magnetic Particles

C. Stamm, F. Marty, A. Vaterlaus, V. Weich, S. Egger, U. Maier, U. Ramsperger, H. Fuhrmann, D. Pescia*

Single two-dimensional (2D) atomically thick magnetic particles of cobalt and iron with variable size and shape were fabricated by combining a mask technique with standard molecular beam epitaxy. Reduction of the lateral size of in-plane magnetized 2D cobalt films down to about 100 nanometers did not essentially modify their magnetic properties; although the separation of boundaries decreased greatly, neither domain penetrated the particle, nor was any sizable shape anisotropy observed. The mutual interaction of 2D cobalt particles was negligible, and the magnetic state of a single particle could be switched without modifying the state of the neighbors. Perpendicularly magnetized iron particles did not exhibit such responses. These results suggest that only a few atoms forming a 2D in-plane magnetized dot may provide a stable elementary bit for nanorecording.

Consider the effects of reducing the lateral dimensions of a magnetic film so that a flat particle is produced. At least two questions arise. First, as the boundaries are coming closer, their demagnetizing action—which is negligibly small, for example, at in-plane magnetized extended films (*1–3*)—is expected to increase. As a result, it might become energetically favorable for domains to penetrate the particle when its lateral size is reduced (*4*). Simultaneously, the shape of the particle (*5–8*) might compete with the magnetocrystalline anisotropy (*9*) to determine the direction of the magnetization M. The second question arises in connection with an ensemble of such particles: The dipolar energy responsible for possible demagnetizing effects within one single particle produces a long-range interaction between the particles. Thus, it might become impossible to change the magnetic state of a particle without affecting the state of the neighbors. As the geometry of the particles and their mutual interaction lead to the complicated magnetic behavior observed in mesoscopic magnets (*4–6, 10–14*), the answers to these two questions are of fundamental importance for possible applications such as magnetic recording.

We addressed these two questions in the limit of atomically thin films of Co on Cu(100). Co/Cu(100) seems to represent a model system for in-plane magnetized ultrathin films (*3, 9, 15–19*) and should provide a suitable reference for starting the patterning operation. The ultraflat particles are produced by molecular beam epitaxy (MBE) (*16, 20*) under ultrahigh-vacuum conditions (10^{-11}-mbar range). Lateral patterning is achieved in situ during MBE by placing a diaphragm between the MBE source and the substrate. This diaphragm consists of a 1-μm-thick foil with microholes that had been etched with a commercial focused ion beam (FIB) system. The magnetization was measured in situ and resolved spatially with two techniques: scanning Kerr microscopy (SKEM, lateral resolution of 1 μm) (*16*) and scanning electron microscopy with polarization analysis (SEMPA, lateral resolution of ~10 nm) (*3, 18, 21, 22*). Sample growth and measurements were performed at room temperature. The thickness of the microstructures was determined by calibrating the evaporation rate with Auger spectroscopy and scanning tunneling microscopy (STM) (*16, 20*) performed on continuous films. On selected microstructures, we cross-checked the thickness by STM. In addition, we used SEMPA to measure the electron spin polarization P as a function of thickness. This allowed an additional thickness calibration that was particularly important for the smallest structures, which turned out to be thinner than expected from the evaporation rate. The sharpness of the boundary of the microstructures, determined by STM, was ~100 nm.

The spatially resolved remanent state magnetization M (zero applied magnetic field H) of ultraflat particles (thickness δ typically in the range 2 AL $< \delta <$ 10 AL, where AL = atomic layer) is shown in Fig. 1 for lateral sizes varying from ~1 mm to ~100 nm. All of the particles are ferromagnetic starting from $\delta \approx 2$ AL; the easy (energetically most favored) M axis is in-plane and along the same crystallographic direction for all of the particles, irrespective of their size and shape. Each particle has a roughly square hysteresis loop (Fig. 1D) with a nearly fully magnetized remanent state, and M is homogeneously distributed; no magnetic domains penetrate the particles even when their size is varied over many decades. A minimum magnetic field H_{rev} is required to switch M of the particles in the opposite direction (see Fig. 1D and the transition from Fig. 1F to Fig. 1G). We studied the magnetic state close to H_{rev}—that is, close to the state of instability toward reversing M—by applying a reverse magnetic field $H_{rev} - \Delta H_{rev}$ (the field was successively switched off to perform the SEMPA imaging). We observed a single-domain state up to reverse applied fields very close to H_{rev} (the smallest values of $\Delta H_{rev}/H_{rev}$ achieved in our study were 0.005). Thus, the microstructures switched from one homogeneous state to the reverse state. With current imaging methods, we are not yet able to determine how this switching (that is, the time evolution of M at H_{rev}) proceeded.

An exception to the single-domain rule is the millimeter-sized Co film seen in Fig. 1B, where millimeter-sized domains are produced in the vicinity of H_{rev}. However, over such large scales, the Co film is bound to meet with the major structural defects provided by the Cu surface and to develop enough magnetostatic energy E_m to create domains and pin their walls. These defects are most likely determining the value of H_{rev} in microstructures as well: H_{rev} increased with thickness (*15*) but did not show any systematic variation with size and shape.

C. Stamm, F. Marty, A. Vaterlaus, V. Weich, S. Egger, U. Maier, D. Pescia, Laboratorium für Festkörperphysik, Eidgenössische Technische Hochschule (ETH) Zürich, CH-8093 Zürich, Switzerland. U. Ramsperger, National Research Institute for Metals, 1-2-1 Sengen, Tsukuba, Ibaraki 305, Japan. H. Fuhrmann, Institut für Teilchenphysik, ETH Zürich, CH-8093 Zürich, Switzerland.

*To whom correspondence should be addressed.